Research Square

Preprints are preliminary reports that have not undergone peer review.
They should not be considered conclusive, used to inform clinical practice,
or referenced by the media as validated information.

Multiparametric quantification of dynamic force adaptation in living cells by atomic force microscopy

Hermann Schillers

schille@uni-muenster.de

University Münster https://orcid.org/0000-0001-6090-4771

Tristan Claus

University Münster https://orcid.org/0009-0001-6009-1464

Dominika Ciechańska

University Münster

Article

Keywords:

Posted Date: October 21st, 2026

DOI: https://doi.org/10.21203/rs.3.rs-10726871/v1

License: This work is licensed under a Creative Commons Attribution 4.0 International License.
Read Full License

Additional Declarations: There is **NO** Competing Interest.

Multiparametric quantification of dynamic force adaptation in living cells by atomic force microscopy

Claus, Tristan Alexander; Ciechańska, Dominika; Schillers, Hermann*

Institute of Physiology 2, University of Münster, Germany

**schille@uni-muenster.de*

Abstract

Living cells continually remodel their mechanical state in response to force, a dynamic behavior that conventional AFM nanoindentation fails to capture and its underlying assumptions are not fully applicable to living cells. Here, we show that TiMeR (Time-Resolved Mechanical Response) provides a model-independent, multiparametric AFM readout of mechanical adaptation by quantifying bidirectional cumulative displacement, work, power, and response balance under constant load. In endothelial cells, TiMeR identifies a stable operating load and resolves distinct, reproducible results following perturbation of mechanosensitive signaling, the cytoskeleton, and inflammatory pathways. TiMeR was also proved applicable to other cell types and can be implemented on conventional AFM platforms without hardware modifications. TiMeR captures biologically informative, time-dependent dimensions of cell mechanics, inaccessible by conventional nanoindentation. Together, these capabilities move cell mechanical characterization beyond static elasticity measurements and establish TiMeR as a powerful tool for uncovering how living cells adapt their mechanical state.

Introduction

Cells continuously experience mechanical forces from the extracellular environment, neighboring cells and tissue deformation, and their ability to sense and adapt to these cues is fundamental to cellular function. Cell mechanics captures this capacity by encompassing both passive properties and active mechanical behavior [1]. Passive properties, defined by elasticity and viscosity, depend on the cytoskeleton, organelles and cytosol [2], whereas cellular mechanical activity includes force generation and relaxation, driven by myosin-based contractility, actin polymerization and cytoskeletal reorganization [3], and

coordinated by mechanotransduction pathways that convert physical cues into intracellular biochemical signals [4]. Mechanical cues are perceived by mechanosensors that are distributed across the cell surface, extracellular matrix, cell–cell junctions and cytoskeleton [5]. In endothelial cells, these include mechanosensitive ion channels such as Piezo [6] and TRPV4 [7], as well as glycocalyx components, GTP-binding proteins, primary cilia, and caveolae [8–10]. These sensors engage multiple signaling pathways including RhoA-ROCK, ERK, Wnt/β-catenin, JAK/STAT, TGFβ/Smad and Hippo-YAP/TAZ signaling and related networks [11,12]. Although many components involved in mechanosensing and force transmission have been identified, the dynamics of the cellular mechanoresponse remain poorly defined [13]. Atomic force microscopy (AFM) is widely used to probe cell mechanics because it combines high force sensitivity with subcellular spatial resolution. In conventional nanoindentation experiments, cells are indented, force-distance curves are recorded, and contact mechanics models are used to estimate elasticity, typically reported as Young's modulus [14]. These measurements are acquired within seconds, using loading forces in the piconewton to low nanonewton range and indentation depths of 100–1000 nm. However, AFM-derived elasticity measurements rely on assumptions of elastic, homogeneous, and isotropic behavior that are not met by living cells [15]. This limitation is substantial because living cells exhibit depth-dependent, nonlinear, and viscoelastic behavior [16]. Moreover, key mechanical responses occur on timescales that overlap with or are shorter than standard indentation measurements. Most AFM-based studies therefore capture a predominantly static endpoint, even though cells respond to mechanical challenge through active and passive processes operating on overlapping timescales. This limitation is particularly relevant as cells respond to mechanical stress in a duration-dependent manner, ranging from an immediate viscoelastic response to large-scale repositioning under prolonged stress (>1 min) [17]. Actin reorganization begins within 10 s of indentation, and cytoskeletal recovery after unloading has a half-life of approximately 14 s [17,18]. Thus, a mechanically active cell can exhibit unchanged apparent elasticity. Conventional AFM nanoindentation therefore captures only a limited and predominantly passive aspect of cell mechanics. Repeated-indentation strategies, force-volume approaches and peak-force nanomechanics [19,20] can probe time-dependent changes, but their recurring load–unload cycles may themselves alter the cellular system under

investigation. Methods that directly resolve how cells adapt under sustained force could therefore broaden AFM-based mechanical phenotyping beyond apparent stiffness. In particular, a constant-force readout that captures how cells rebalance opposing components of the response over time would provide access to a dimension of cell mechanics that is only partly reflected by conventional nanoindentation measurements.

Here, we show that TiMeR, an AFM-based method that records cell height over time under constant load, quantifies bidirectional mechanical adaptation through cumulative displacement and power. The approach is based on force-clamp indentation and the simultaneous real-time recording of piezo displacement, which directly reflects changes in cell height with a temporal resolution of 0.01 s. Because TiMeR relies on direct time-resolved displacement measurements under sustained force, its primary readout does not depend on fitted contact-mechanics assumptions. Using fixed cell and substrate controls, we first establish that the measured signal is specific to living cells. We then apply the method in living endothelial cells to define a stable operating load and distinguish phenotypes across cytoskeletal, mechanosensitive signaling and inflammatory perturbations. Together, these considerations position TiMeR as a practical, model-independent framework for quantifying dynamic force adaptation and generating readouts that can help uncover its underlying mechanisms.

Results

TiMeR captures living-cell-specific mechanical dynamics

To determine whether TiMeR captures living-cell-specific mechanical activity, we compared recordings obtained under constant load from living HMEC-1 cells, PFA-fixed cells and cell-free culture dishes. Representative traces shown in Fig. 1a revealed substantially larger bidirectional height fluctuations in living cells (blue trace), whereas PFA-fixed cells (red trace) and dish-only controls (green trace) remained close to baseline throughout the recording period. Positive slopes indicate upward displacement and a push against the indenter, whereas negative slopes indicate downward displacement and cell relaxation. For quantification, instrumental noise in TiMeR recordings was reduced using a Savitzky-Golay filter, which balanced noise suppression with signal preservation. Each trace was then summarized by two values, the cumulative upward and downward height changes under

constant load over 150 s, termed dynamic response amplitudes (DRA). Accordingly, the mechanical response of a single cell is represented by one positive, push-associated (+DRA) and one negative, relaxation-related (-DRA) dynamic response amplitude. Living HMEC-1 cells displayed markedly larger bidirectional DRAs than fixed cells or dish-only controls, with median values of -416 nm and +283 nm, compared with -137 nm and +82 nm for fixed cells and -57 nm and +60 nm for dish-only controls (Fig. 1b). By comparison, conventional nanoindentation showed that fixation increased the median Young's modulus from 984 Pa to 1618 Pa (Fig. 1c). Together, these data show that TiMeR captures dynamic height fluctuations that are characteristic of living cells and strongly reduced after fixation.

Load dependence defines an operating range for TiMeR measurements

To define an operating load for TiMeR measurements, HMEC-1 cells were recorded under constant forces ranging from 300 to 1500 pN. Across this range, +DRA decreased with increasing force, whereas -DRA showed no comparably monotonic trend (Fig. 2a). At 300 pN, cells displayed the largest median DRAs, but cantilever tracking was frequently lost during the 150-s recording period. At intermediate loads of 400 and 600 pN, tracking remained stable while substantial bidirectional height changes were preserved. At higher loads of 800–1500 pN, positive DRAs were reduced, whereas negative DRAs remained prominent. Fig. 2a shows the full dataset but does not display the single-cell ratios of the two TiMeR response components, -DRA and +DRA. However, the relationship between push and relaxation at the single-cell level is crucial for evaluating force dependence, and calculating ratios for each recording avoids distortions that can arise from group medians. To capture this balance at the single-cell level, we calculated the ratio of negative to positive DRA for each recording. From 300 to 600 pN, this ratio remained relatively stable at approximately 1.4–1.5. At higher loads, the ratio shifted progressively toward negative DRA, indicating that the relative contribution of the two response components changed with increasing force (Fig. 2b). On this basis, 600 pN was selected as the operating force for subsequent experiments.

Perturbation of the actomyosin network shifts cellular mechanodynamics toward relaxation

To assess how the actomyosin network contributes to TiMeR-derived mechanodynamics, filamentous actin was disrupted with cytochalasin D and non-muscle myosin II was inhibited with blebbistatin. Both perturbations shifted the response toward relaxation, with increased relaxation-associated DRA and reduced push-associated DRA relative to vehicle-treated control cells (Fig. 3a). This shift was strongest after cytochalasin D treatment, whereas blebbistatin produced a less pronounced but still substantial change in response balance. While the dynamic response amplitude describes the overall extent of height fluctuations, TiMeR recordings also allow analysis of their kinetics because both displacement and duration can be resolved at high temporal resolution. To capture this aspect, median cellular power output was calculated by dividing cumulative mechanical work (force × displacement) by the duration of the respective upward or downward phases. Both treatments increased relaxation-associated power, from -3.1 aW in control cells to -5.8 aW after blebbistatin and -8.5 aW after cytochalasin D (Fig. 3b). Push-associated power also increased modestly, from 2.1 aW in control cells to 2.5 aW after blebbistatin and 2.6 aW after cytochalasin D. Analogous to the ratio of DRAs, we calculated the ratio of power to capture the mechanodynamic balance at the single-cell level. Despite the increase in push-associated power, the larger rise in relaxation-associated power resulted in a marked shift in the power ratio, which increased from 1.4 in control cells to 2.1 after blebbistatin and 3.2 after cytochalasin D (Fig. 3c). To benchmark these TiMeR-derived phenotypes against a conventional mechanical readout, AFM nanoindentation measurements were performed under the same perturbation conditions. Both actomyosin perturbations reduced apparent cell elasticity, with median Young's modulus values decreasing from 960 Pa in control cells to 704 Pa after blebbistatin treatment and 279 Pa after cytochalasin D treatment (Fig. 3d).

Mechanosensor and ROCK pathway perturbation alter cellular mechanodynamics

To assess how mechanosensitive signaling and ROCK activity contribute to TiMeR-derived mechanodynamics, we performed measurements after pharmacological activation of PIEZO1 with Yoda1, inhibition of mechanosensitive ion channels with GsMTx4 and inhibition of the RhoA-ROCK pathway (RhoA, Ras homolog family member A; ROCK, Rho-associated, coiled-coil containing protein kinase) with H-1152. To account for solvent

effects, Yoda1-treated cells were compared with the DMSO-containing control (DMSO), whereas GsMTx4- and H-1152-treated cells were compared with the solvent-free control (HMEC-1). Yoda1 increased relaxation-associated DRA while leaving push-associated DRA largely unchanged relative to the DMSO-containing control (Fig. 4a). GsMTx4, by contrast, reduced push-associated DRA with comparatively minor effects on the relaxation-associated component, whereas H-1152 attenuated both components, yielding a profile comparable to that observed after GsMTx4 treatment (Fig. 4a). We next quantified the corresponding power readouts. Yoda1 increased relaxation-associated power with only minor effects on push-associated power, whereas GsMTx4 and H-1152 reduced both components to a similar extent (Fig. 4b). At the single-cell level, the power ratio remained similar to control after Yoda1 treatment, whereas GsMTx4 and H-1152 each produced a small but significant increase, indicating a modest shift in mechanodynamic balance driven by disproportionate loss of push-associated output rather than an absolute increase in relaxation (Fig. 4c). AFM nanoindentation under identical conditions detected a significant decrease in median Young's modulus only after H-1152 treatment (578 Pa), while Yoda1- and GsMTx4-treated cells were indistinguishable from controls (Fig. 4d). TiMeR, by contrast, resolved distinct, reproducible changes in dynamic response amplitude and power across all three treatments. Thus, TiMeR reveals signaling-dependent dynamic force-adaptation phenotypes that remain undetected by indentation-derived apparent elasticity.

TNF-α reshapes endothelial mechanodynamics

To determine how inflammatory stimulation affects endothelial mechanodynamics, TiMeR measurements were performed on HMEC-1 cells after 24 h treatment with TNF-α. TNF-α selectively reduced push-associated DRA by 32%, from 283 nm in control cells to 193 nm after treatment, whereas relaxation-associated DRA remained similar to that of untreated control cells (−381 versus −416 nm; Fig. 5a). These data indicate that inflammatory stimulation primarily impairs the push-associated component of the response rather than increasing the relaxation-associated component. We next quantified the corresponding power readouts. TNF-α reduced push-associated power by approximately 25%, from 2.5 aW to 1.9 aW, whereas relaxation-associated power remained similar to control values

(−2.6 versus −3.1 aW; Fig. 5b). Consistent with this shift, the power ratio increased from 1.2 in control cells to 1.4 after TNF-α treatment, indicating a relative shift in mechanodynamic balance toward relaxation driven by reduced pushing capacity (Fig. 5c).

To compare these TiMeR-derived changes with a conventional mechanical readout, AFM nanoindentation measurements were performed under the same conditions. TNF-α increased apparent cell elasticity, with the median Young's modulus rising from 984 Pa in control cells to 1208 Pa after treatment (Fig. 5d). In contrast, TiMeR revealed a concomitant loss of the push-associated dynamic response. Apparent stiffness alone thus fails to discriminate inflammatory stiffening from the concurrent remodeling of dynamic force adaptation.

To examine whether the TNF-α-induced mechanodynamic changes were accompanied by structural alterations, immunofluorescence microscopy was performed on untreated and TNF-α-treated HMEC-1 cells (Fig. 6). Untreated control cells exhibited only sporadic actin stress fibers and low basal VCAM1 immunofluorescence signal (Fig. 6a), whereas TNF-α-treated cells showed pronounced actin stress fiber formation throughout the cell body together with markedly increased VCAM1 immunofluorescence signal (Fig. 6b). These findings indicate that the altered TiMeR phenotype is accompanied by cytoskeletal remodeling and endothelial activation.

TiMeR resolves cell-line-specific mechanodynamic profiles

To assess the applicability of TiMeR beyond endothelial cells, measurements were performed at a constant load of 600 pN in Panc-1, BxPC-3, and PC-9 cancer cells. All cell lines exhibited robust bidirectional height responses, confirming the applicability of TiMeR across distinct cell types. TiMeR resolved distinct mechanodynamic profiles among the four independent cell lines. Panc-1 cells exhibited the largest negative and positive dynamic response amplitudes (−971/+467 nm) and power values (−6.4/+4.3 aW). PC-9 cells showed a similarly pronounced negative response (−944 nm; −5.5 aW), but lower positive amplitude and power (+173 nm; +2.4 aW), indicating a relative predominance of the negative response component. In contrast, HMEC-1 and BxPC-3 cells displayed lower response amplitudes and power values (Fig. 7a,b). Consistently, the negative-to-positive

power ratio was highest in PC-9 cells (2.2), exceeding that of BxPC-3 (1.6), Panc-1 (1.3), and HMEC-1 cells (1.2) (Fig. 7c). HMEC-1 and Panc-1 cells displayed low ratios of 1.2 and 1.3, respectively, consistent with a comparatively balanced contribution of negative and positive power. Thus, TiMeR distinguishes cell-line-specific phenotypes in both the magnitude and relative balance of dynamic force adaptation.

Together, TiMeR provides a multiparametric mechanodynamic profile — comprising bidirectional displacement, power, and their ratio — that distinguishes phenotypes invisible to elasticity measurements.

Discussion

The curves in Fig. 1a provide an initial validation of TiMeR by demonstrating that pronounced bidirectional height fluctuations under a constant load are a characteristic feature of living cells. The bidirectional height changes in living cells exceeded the signal obtained on fixed cells by more than a factor of three, indicating that the observed dynamics are dominated by living-cell behavior rather than instrumental drift alone. The residual amplitudes observed in cell-free dishes most likely reflect instrumental and environmental background after smoothing, whereas the slightly larger and predominantly negative amplitudes in fixed cells are consistent with passive time-dependent processes such as poroelastic relaxation in a structurally preserved but biologically inactive cell [21]. Rather than describing the cell primarily through a static elasticity readout, TiMeR resolves how living cells adapt mechanically over time under sustained load by quantifying the bidirectional mechanical activity of the response. This divergence is conceptually important: fixation increases apparent elasticity but simultaneously suppresses the large bidirectional fluctuations observed in living cells, showing that elasticity and dynamic force adaptation are related but clearly separable features of cell mechanics. Together, our data show that TiMeR captures a dimension of cell mechanics that is only partly represented by conventional AFM nanoindentation and apparent elasticity measurements.

The load-dependence experiments further show that TiMeR responses are shaped by the interplay between the applied force and the cell’s capacity to maintain bidirectional activity.

Across the range from 300 to 600 pN, the ratio of -DRA to +DRA remained relatively stable, whereas at higher loads the balance shifted toward negative DRA. This pattern argues against a trivial interpretation in which stronger force simply scales the same response. Instead, the response architecture itself changes as loading increases, indicating that the cell transitions from a balanced regime with maintained push and relaxation to a regime dominated by yielding. Within this framework, lower applied forces preserve a state in which cells can both yield and actively counteract the indenter, whereas higher loads progressively restrict active push and favor mechanical evasion or yielding. This shift may reflect a protective adaptation that limits excessive strain under stronger sustained force. The identification of 600 pN as a stable operating point is therefore not only practical but mechanistically meaningful.

The actomyosin perturbation experiments show that balanced mechanodynamics depend on both cortical integrity and contractile activity. The actomyosin cortex is a central component of cellular tensegrity, providing structural resistance and active countertension under load [22,23]. Filamentous actin is the structural scaffold of the cortex, whereas myosin II-dependent contractility generates and stabilizes cortical tension [24,25]. Consistent with this, disruption of filamentous actin with cytochalasin D or inhibition of non-muscle myosin II with blebbistatin each shifted the TiMeR response toward relaxation-associated behavior, with the strongest effect observed after cytochalasin D treatment. The stronger effect of cytochalasin D compared with blebbistatin is consistent with the central role of filamentous actin in both myosin-dependent force generation and mechanical integrity under load. Analysis of power further showed that both perturbations do not simply suppress the measurable mechanical output, but instead shifted the response toward the relaxation-associated component, despite only modest changes in push-associated power.

The combination of reduced positive DRA and modestly increased positive power suggests that the remaining upward movements differ qualitatively from the push response observed in control cells. This may instead reflect faster, recoil-like displacements driven by the release of stored elastic strain energy from residual cellular structures rather than active force generation [26]. TiMeR is particularly informative here because it reveals changes not only in response magnitude, but also in response balance and kinetics, features that are not captured by the single endpoint stiffness value provided by conventional

nanoindentation. The accompanying reduction in apparent elasticity further shows that this relaxation-shifted mechanodynamic phenotype occurs together with substantial softening. These findings indicate that an intact actomyosin cortex is required not only for resistance to deformation, but also for maintaining a balanced dynamic response under sustained force.

Adaptive mechanical responses to sustained load require not only a functional contractile cytoskeleton, but also the ability of cells to detect mechanical cues and transduce them into intracellular signals that regulate cytoskeletal remodeling and force generation. In endothelial cells, mechanosensitive ion channels such as PIEZO1 are key components of this process [27], whereas downstream RhoA-ROCK signaling links force perception to cytoskeletal rearrangement and actomyosin contractility [28]. Briefly, activation of PIEZO1 by membrane deformation results in calcium influx that activates RhoA-specific guanine nucleotide exchange factors, which in turn activate ROCK [29]. Within this framework, the mechanosensor and ROCK perturbations further indicate that TiMeR can resolve distinct signaling-dependent response phenotypes. PIEZO1 activation with Yoda1 selectively enhanced the relaxation-associated component while largely preserving the push-associated component; because Yoda1 does not directly disrupt the actomyosin cortex, cells retain the capacity to actively push against the cantilever despite an increased tendency to relax, consistent with the interpretation that pharmacological PIEZO1 stimulation causes the cell to perceive a mechanical challenge stronger than that exerted by the indenter [30]. GsMTx4-mediated partial inhibition of PIEZO1 [31] selectively reduced the push-associated response, whereas H-1152 attenuated both dynamic response components, consistent with the broad role of ROCK in regulating actomyosin contractility, cortical tension, and cytoskeletal organization [1,28]. Importantly, these perturbations were only incompletely captured by AFM nanoindentation: apparent cell elasticity remained unchanged following Yoda1 and GsMTx4 treatment and was altered only after ROCK inhibition. In contrast, TiMeR resolved distinct and reproducible mechanodynamic phenotypes under all three conditions. This difference reflects the fundamentally greater information content of the TiMeR readout. Whereas nanoindentation reduces the mechanical response to a single quasi-static estimate of apparent elasticity, TiMeR quantifies the negative and positive dynamic response amplitudes, their associated power

outputs, and the balance between both response phases. TiMeR thereby captures both the magnitude and temporal asymmetry of cellular force adaptation, enabling the discrimination of phenotypes that remain indistinguishable by apparent elasticity alone. Accordingly, TiMeR provides higher phenotypic resolution than indentation-derived elasticity measurements for signaling-dependent mechanical perturbations. The Yoda1 phenotype is consistent with altered mechanosensitive signaling, whereas GsMTx4 reduced the push-associated component, consistent with attenuated mechanosensitive channel input. In contrast, the broad reduction of both dynamic response components following H-1152 is consistent with impaired ROCK-dependent cytoskeletal force generation and remodeling. The finding that Yoda1 and GsMTx4 induced pronounced TiMeR phenotypes without detectable changes in apparent elasticity demonstrates that dynamic force adaptation can be extensively remodeled in the absence of a proportional change in quasi-static stiffness. Thus, by providing a multidimensional mechanodynamic profile rather than a single stiffness value, TiMeR reveals functional consequences of signaling perturbations that conventional AFM nanoindentation does not resolve.

The TNF-α experiments extend this principle to an inflammatory context by showing that inflammatory activation selectively reshapes endothelial mechanodynamics. The endothelium regulates vascular tone, blood flow, inflammatory responses and permeability through the coordinated interplay of mechanical cues, such as shear stress and pulsatile pressure, and biochemical signaling pathways [32]. During inflammation, endothelial cells integrate these inputs with cell-generated forces, leading to cytoskeletal remodeling and altered contractility, which in turn influence vascular permeability, leukocyte trafficking, cytokine production and vascular remodeling [33–35]. TNF-α is a central proinflammatory cytokine and an established mediator of endothelial dysfunction [36]. In this endothelial model, TNF-α selectively reduced the push-associated dynamic response, as reflected by decreased positive DRA and power, while the negative, relaxation-associated components remained largely unchanged (Fig. 5a,b). Consequently, the ratio of negative to positive power increased, indicating a shift in mechanodynamic balance towards relative dominance of the relaxation-associated response (Fig. 5c). This phenotype is consistent with TNF-α-induced actomyosin remodeling. TNF-α promotes the formation of contractile actin stress fibres and increases centripetal tension, which may reduce the capacity of cells

to generate an outward-directed counterresponse while preserving time-dependent relaxation [37–39]. Accordingly, TNF-α-treated cells displayed more prominent phalloidin-labelled stress fibres and increased VCAM1 immunofluorescence, consistent with cytoskeletal remodeling and endothelial activation (Fig. 6) [40,41]. Although these microscopy observations are qualitative, they provide morphological context for the TiMeR phenotype.

Importantly, AFM nanoindentation detected only an increase in apparent elasticity following TNF-α treatment (Fig. 5d). This single quasi-static elasticity measure does not reveal that the increase in apparent stiffness coincides with a selective loss of push-associated dynamic force adaptation. In contrast, TiMeR resolves the amplitude, power, and relative balance of the negative and positive response phases, thereby providing a multidimensional mechanodynamic profile of inflammatory remodeling. Thus, TiMeR distinguishes inflammatory stiffening from the concurrent impairment of active force adaptation—information that is inaccessible from apparent elasticity alone.

Together with the cytoskeletal and mechanosensory perturbation experiments, these findings support cellular mechanodynamics as an operational framework for describing adaptive responses to sustained force. In this framework, push and relaxation represent integrated outputs of contractility, cortical organization, mechanosensitive signaling, and time-dependent relaxation rather than isolated molecular mechanisms. TiMeR therefore extends AFM-based mechanical phenotyping beyond static indentation-derived elasticity by resolving dynamic force adaptation as a distinct and information-rich dimension of cell mechanics.

Beyond describing perturbation-specific phenotypes, TiMeR places cellular force adaptation on a quantitative energetic scale, further supporting the biological relevance of the readout. At 600 pN, the median positive displacement in untreated cells corresponds to about 170 aJ of work. Assuming an energy yield of approximately 80×10^{-21} J per ATP hydrolysis under physiological conditions and ideal coupling efficiency, this corresponds to a minimum of roughly 2,000–3,000 ATP molecules. Although not a direct measure of ATP consumption, this places the TiMeR readout on an energetic scale that highlights its sensitivity to very small amounts of cellular mechanical output. The scale is also consistent

with molecular motor mechanics, for example the coupling of one ATP hydrolysis event to an 8-nm kinesin step [42], and thus provides a conceptual link between cellular mechanics and the energetic cost of force adaptation.

The cell-line comparison demonstrates that TiMeR is applicable beyond the endothelial context. Using the same measurement protocol, Panc-1, BxPC-3, and PC-9 cells exhibited distinct dynamic response amplitudes, displacement-derived power values, and negative-to-positive power ratios relative to HMEC-1 cells (Fig. 7a–c). These findings indicate that baseline mechanodynamic behaviour varies across the cell lines examined. Because the cancer cell lines differ from HMEC-1 cells in tissue origin, cell state, morphology, and cytoskeletal organisation, these factors may contribute to the observed differences; however, defining their individual contributions was beyond the scope of this baseline characterisation. Nevertheless, the robust and statistically distinguishable profiles obtained across all four cell lines support the broader applicability of TiMeR for mechanodynamic phenotyping in living cells.

Several limitations should be considered. TiMeR provides an integrated readout of cellular adaptation to sustained load and does not directly resolve the molecular processes underlying each response component. Accordingly, positive and negative DRA, as well as their associated power values, should be interpreted as composite mechanical outputs whose relative contributions may differ between cell types and perturbations. In combination with targeted pharmacological, genetic, or imaging-based approaches, however, TiMeR can help relate these mechanodynamic phenotypes to the cellular pathways that regulate force adaptation.

Taken together, TiMeR establishes dynamic force adaptation as a biologically informative dimension of cell mechanics that is distinct from and inaccessible to apparent elasticity. By quantifying bidirectional displacement, power, and the balance between response phases, TiMeR provides substantially greater phenotypic information than conventional nanoindentation, which yields a single quasi-static estimate of apparent elasticity. TiMeR detected mechanodynamic phenotypes associated with mechanosensitive-channel perturbation, ROCK inhibition, and inflammatory activation that were either not detected or only incompletely represented by indentation-derived stiffness measurements. As the

assay can be implemented on conventional AFM platforms without hardware modification and applied across endothelial and non-endothelial cell lines, TiMeR provides a practical framework for investigating how living cells generate, redistribute, and rebalance mechanical output under sustained load.

Methods

Cell culture

Human microvascular endothelial cells (HMEC-1; RRID: CVCL_0307), human ductal pancreatic cancer cells (PANC-1; RRID: CVCL_0480), pancreatic adenocarcinoma cells (BxPC-3; RRID: CVCL_0186) and human lung adenocarcinoma cells (PC-9; RRID: CVCL_B260) were cultured in RPMI 1640 supplemented with 10% fetal bovine serum and 1% penicillin-streptomycin in a humidified incubator at 37 °C and 5% CO_2. Cells from passages 9–15 were used at 80–90% confluence for AFM measurements. For endothelial activation, cells were treated with TNF-α at 10 ng ml^{-1} for 24 h. Actin polymerization was inhibited with cytochalasin D at 600 nM for 15 min, non-muscle myosin II activity was inhibited with blebbistatin at 25 μM for 120 min, PIEZO1 was activated with Yoda1 at 1 μM for 30 min, mechanosensitive ion channels were inhibited with GsMTx4 at 50 nM for 30 min and ROCK was inhibited with H-1152 at 100 nM for 30 min. For fixed-cell experiments, cells were incubated with 4% paraformaldehyde for 15 min at room temperature.

Atomic force microscopy

Nanoindentation and TiMeR measurements were conducted using a BioScope Resolve atomic force microscope operated in closed-loop contact mode. Cells were measured in Leibovitz medium supplemented with 1% fetal bovine serum and 1% penicillin-streptomycin at 37 °C, using an evaporation-prevention cover and an active anti-vibration platform to minimize background noise. Drift-compensated spherical probes (MLCT-SPH-5UM-DC; Bruker AFM Probes, Camarillo, USA) with a tip radius of 4.9 μm and spring constants of 0.015–0.017 N m^{-1} were used. Deflection sensitivity was calibrated before testing according to a standardized nanomechanical AFM procedure.

For nanoindentation experiments, force-distance curves were acquired with a mechanical load of 600 pN and a tip velocity of 1 μm s^{-1}. Each curve was analyzed individually using the linearized Hertz model for spherical indenters in PUNIAS software to determine Young's modulus over the 100–600 pN loading range, corresponding to an indentation depth of approximately 200 nm. For TiMeR measurements, a custom-built script in the Ramp Script Editor of NanoScope software was used. The indenter was positioned over the nuclear region and brought into contact at 1 μm s^{-1} until a force of exactly 600 pN was reached. This force was then maintained for 150 s while the vertical piezo displacement was recorded in real time at 100 Hz, followed by probe retraction. A MATLAB script was used to compute parameters including total height change, work and power from the vertical displacement traces.

Data processing of TiMeR measurements

In constant-force AFM measurements, the instrument maintains a defined cantilever deflection corresponding to the target force according to Hooke's law. When the cell relaxes and cantilever bending decreases, the piezo elongates to restore the target deflection; when the cell pushes against the cantilever and cantilever bending increases, the piezo compensates by contracting. In the BioScope Resolve configuration used here, positive piezo movement therefore represents cellular relaxation and negative piezo movement represents a push against the indenter. Height traces were smoothed using a Savitzky-Golay filter with a 499-point window to reduce instrumental noise. After smoothing, the first derivative at each 0.01-s interval was calculated to determine both the magnitude and timing of local height changes. Positive and negative height changes were summed separately to obtain the total height changes in both directions. For visual presentation, the sign was inverted so that pushes are displayed as positive values and relaxations as negative values. Power was calculated from applied force, displacement and time according to the formula Power = Force × Displacement / Time.

Immunofluorescence microscopy

To assess actin cytoskeletal remodeling and confirm endothelial activation, immunofluorescence microscopy was performed on untreated control cells and cells treated with 10 ng ml^{-1} TNF-α for 24 h. Cells were cultured in 4-well tissue culture chambers (94.6170.402; Sarstedt) until 80% confluence, then fixed with 4% PFA for 15 min and

permeabilized with 0.1% Triton X-100 for 10 min at room temperature. After blocking with 5% bovine serum albumin (BSA; Serva) for 30 min at room temperature, cells were incubated overnight at 4 °C in PBS supplemented with 0.5% BSA containing the following markers: nuclear staining with 4’,6-diamidino-2-phenylindole (DAPI; D1306; Invitrogen) at 1:2000 dilution, filamentous actin labeling with Phalloidin–Alexa Fluor 488 (A12379; Invitrogen) at 1:1000, and a rabbit monoclonal antibody detecting VCAM1 (RRID: AB_2721053; Abcam) at 1:250 dilution. The next day, cells were washed and incubated with Alexa Fluor 647-conjugated secondary goat anti-rabbit IgG $F(ab')_2$ (RRID: AB_2338082; Jackson ImmunoResearch) at 1:1000 dilution for 1 h at room temperature in PBS containing 0.5% BSA. After staining, slides were washed and covered in fluorescence mounting medium (S3023; Agilent). Imaging was performed on a Nikon ECLIPSE Ti2 confocal microscope using a 60× oil immersion objective (Plan Apo Lambda, NA 1.40). Data were acquired using NIS-Elements software (version 5.30.07). Brightness and contrast were adjusted linearly for display purposes only; no other image manipulations were performed.

Statistical analysis

Statistical analyses and data visualization were performed using GraphPad Prism version 8.43. For each experiment, 26–131 curves were acquired from 2–4 culture dishes on independent experimental days. Datasets were compared using the Mann-Whitney U test, with statistical significance defined as $p < 0.05$ and indicated by standard asterisk notation *$p < 0.05$; **$p < 0.01$; ***$p < 0.001$; ****$p < 0.0001$. Data are presented as box plots with individual points, median values and interquartile ranges.

Data availability

The data supporting the findings of this study, including the source data underlying Figures 1–7, are available from the corresponding author upon reasonable request.

Code availability

The custom MATLAB and NanoScope Ramp Script Editor scripts used to acquire and process TiMeR measurements are available from the corresponding author upon reasonable request.

Funding

T.A.C. was supported by a scholarship from the Medical Faculty of the University of Münster (240022; Medizinerkolleg-MedK) and by a scholarship from the German Academic Scholarship Foundation (392677; Studienstiftung des deutschen Volkes). The project was supported by the
European Union's Horizon 2020 Research and Innovation Programme, project Phys2BioMed (812772), under a Marie Skłodowska-Curie grant.

Author contributions

T.A.C. conceived and conducted experiments, analyzed data and wrote the manuscript; D.C. performed experiments and analyzed data; H.S. supervised the project, acquired funding and revised the manuscript.

Competing interests

The authors declare no competing interests.

Ethics

No animal experiments were conducted and no patient data were used.

References

1. Fletcher, D. A. & Mullins, R. D. Cell mechanics and the cytoskeleton. *Nature* **463**, 485–492 (2010).
2. Runel, G., Lopez-ramirez, N., Chlasta, J. & Masse, I. Biomechanical Properties of Cancer Cells. *Cells* **10**, 887 (2021).
3. Ahmed, W. W., Fodor, É. & Betz, T. Active cell mechanics: Measurement and theory. *Biochim. Biophys. Acta Mol. Cell Res.* **1853**, 3083–3094 (2015).
4. Jaalouk, D. E. & Lammerding, J. Mechanotransduction gone awry. *Nat. Rev. Mol. Cell Biol.* **10**, 63–73 (2009).
5. Janmey, P. A. & McCulloch, C. A. Cell mechanics: Integrating cell responses to mechanical stimuli. *Annu. Rev. Biomed. Eng.* **9**, 1–34 (2007).
6. Lacroix, J. J. & Wijerathne, T. D. PIEZO channels as multimodal mechanotransducers. *Biochem. Soc. Trans.* **53**, 293–301 (2025).

7. Martinac, B. & Poole, K. Mechanically activated ion channels. *Int. J. Biochem. Cell Biol.* **97**, 104–107 (2018).

8. Askari, H., Sadeghinejad, M. & Fancher, I. S. Mechanotransduction and the endothelial glycocalyx: Interactions with membrane and cytoskeletal proteins to transduce force. *Curr. Top. Membr.* **91**, 43–60 (2023).

9. Xu, J. *et al.* GPR68 Senses Flow and Is Essential for Vascular Physiology. *Cell* **173**, 762-775.e16 (2018).

10. Iomini, C., Tejada, K., Mo, W., Vaananen, H. & Piperno, G. Primary cilia of human endothelial cells disassemble under laminar shear stress. *J. Cell Biol.* **164**, 811– 817 (2004).

11. Di, X. *et al.* Cellular mechanotransduction in health and diseases: from molecular mechanism to therapeutic targets. *Signal Transduct. Target. Ther.* **8**, 1–32 (2023).

12. Mierke, C. T. Mechanosensory entities and functionality of endothelial cells. *Front. Cell Dev. Biol.* **12**, 1446452 (2024).

13. Bril, M., Fredrich, S. & Kurniawan, N. A. Stimuli-responsive materials: A smart way to study dynamic cell responses. *Smart Mater. Med.* **3**, 257–273 (2022).

14. Rotsch, C., Jacobson, K. & Radmacher, M. Dimensional and mechanical dynamics of active and stable edges in motile fibroblasts investigated by using atomic force microscopy. *Proc. Natl. Acad. Sci. U. S. A.* **96**, 921–926 (1999).

15. Pérez-Domínguez, S. *et al.* Reliable, standardized measurements for cell mechanical properties. *Nanoscale* **15**, 16371–16380 (2023).

16. Kontomaris, S. V., Malamou, A. & Stylianou, A. A New Approach for the AFM-Based Mechanical Characterization of Biological Samples. *Scanning* **2020**, 2896792 (2020).

17. Matthews, B. D., Overby, D. R., Mannix, R. & Ingber, D. E. Cellular adaptation to mechanical stress: role of integrins, Rho, cytoskeletal tension and mechanosensitive ion channels. *J. Cell Sci.* **119**, 508–518 (2006).

18. Shao, X., Li, Q., Mogilner, A., Bershadsky, A. D. & Shivashankar, G. V. Mechanical stimulation induces formin-dependent assembly of a perinuclear actin rim. *Proc. Natl. Acad. Sci. U. S. A.* **112**, E2595–E2601 (2015).

19. Hu, J., Chen, S., Hu, W., Lü, S. & Long, M. Mechanical Point Loading Induces Cortex Stiffening and Actin Reorganization. *Biophys. J.* **117**, 1405–1418 (2019).

20. Schillers, H., Wälte, M., Urbanova, K. & Oberleithner, H. Real-time monitoring of cell elasticity reveals oscillating myosin activity. *Biophys. J.* **99**, 3639–3646 (2010).

21. Schillers, H., Medalsy, I., Hu, S., Slade, A. L. & Shaw, J. E. PeakForce Tapping resolves individual microvilli on living cells. *J. Mol. Recognit.* **29**, 95–101 (2016).

22. Moeendarbary, E. *et al.* The cytoplasm of living cells behaves as a poroelastic material. *Nat. Mater.* **12**, 253–261 (2013).

23. Ingber, D. E. Tensegrity and mechanotransduction. *J. Bodyw. Mov. Ther.* **12**, 198–200 (2008).

24. Klingner, C. *et al.* Isotropic actomyosin dynamics promote organization of the apical cell cortex in epithelial cells. *J. Cell Biol.* **207**, 107–121 (2014).

25. Vicente-Manzanares, M., Ma, X., Adelstein, R. S. & Horwitz, A. R. Non-muscle myosin II takes centre stage in cell adhesion and migration. *Nat. Rev. Mol. Cell Biol.* **10**, 778–790 (2009).

26. Kelkar, M., Bohec, P. & Charras, G. Mechanics of the cellular actin cortex: From signalling to shape change. *Curr. Opin. Cell Biol.* **66**, 69–78 (2020).

27. Gurmessa, B., Ricketts, S. & Robertson-Anderson, R. M. Nonlinear Actin Deformations Lead to Network Stiffening, Yielding, and Nonuniform Stress Propagation. *Biophys. J.* **113**, 1540–1550 (2017).

28. Douguet, D., Patel, A., Xu, A., Vanhoutte, P. M. & Honoré, E. Piezo Ion Channels in Cardiovascular Mechanobiology. *Trends Pharmacol. Sci.* **40**, 956–970 (2019).

29. Olson, M. F. Rho-associated coiled-coil containing kinases (ROCK): structure, regulation, and functions. *Small GTPases* **5**, e29846 (2014).

30. Pardo-Pastor, C. *et al.* Piezo2 channel regulates RhoA and actin cytoskeleton to promote cell mechanobiological responses. *Proc. Natl. Acad. Sci. U. S. A.* **115**, 1925–1930 (2018).

31. Syeda, R. *et al.* Chemical activation of the mechanotransduction channel Piezo1. *elife* **4**, e07369 (2015).

32. Bae, C., Sachs, F. & Gottlieb, P. A. The mechanosensitive ion channel Piezo1 is inhibited by the peptide GsMTx4. *Biochemistry* **50**, 6295-6300 (2011).

33. Sena, C. M., Pereira, A. M. & Seiça, R. Endothelial dysfunction - A major mediator of diabetic vascular disease. *Biochim. Biophys. Acta Mol. Basis Dis.* **1832**, 2216–2231 (2013).

34. Bryan, M. T. *et al.* Mechanoresponsive networks controlling vascular inflammation. *Arterioscler. Thromb. Vasc. Biol.* **34**, 2199–2205 (2014).

35. Fels, J. & Kusche-Vihrog, K. Endothelial Nanomechanics in the Context of Endothelial (Dys)function and Inflammation. *Antioxid. Redox Signal.* **30**, 945–959 (2019).

36. Dri, E. *et al.* Inflammatory mediators of endothelial dysfunction. *Life* **13**, 1420 (2023).

37. Zhang, H. *et al.* Role of TNF-α in vascular dysfunction. *Clin. Sci. (Lond).* **116**, 219-230 (2009).

38. Prasain, N. & Stevens, T. The actin cytoskeleton in endothelial cell phenotypes. *Microvasc. Res.* **77**, 53-63 (2008).

39. Hotulainen, P. & Lappalainen, P. Stress fibers are generated by two distinct actin assembly mechanisms in motile cells. *J. Cell Biol.* **173**, 383–394 (2006).

40. Dudek, S. M. & Garcia, J. G. N. Cytoskeletal regulation of pulmonary vascular permeability. *J. Appl. Physiol. (1985)* **91**, 1487–1500 (2001).

41. Aldirawi, M. *et al.* A specific role for endothelial EPLIN-isoform-regulated actin dynamics in neutrophil transmigration. *Sci. Rep.* **15**, 15698 (2025).

42. Jia, Z. *et al.* Luteolin protects against vascular inflammation in mice and TNF-alphainduced monocyte adhesion to endothelial cells via suppressing IκBα/NF-κB signaling pathway. *J. Nutr. Biochem.* **26**, 293–302 (2015).

43. Lee, S. Y. *et al.* Probing the mechanical properties of TNF-α stimulated endothelial cell with atomic force microscopy. *Int. J. Nanomedicine* **6**, 179–195 (2011).

44. Stroka, K. M., Vaitkus, J. A. & Aranda-Espinoza, H. Endothelial cells undergo morphological, biomechanical, and dynamic changes in response to tumor necrosis factorα. *Eur. Biophys. J.* **41**, 939-947 (2012).

45. Schnitzer, M. J. & Block, S. M. Kinesin hydrolyses one ATP per 8-nm step. *Nature* **388**, 386–390 (1997).

Figure 1

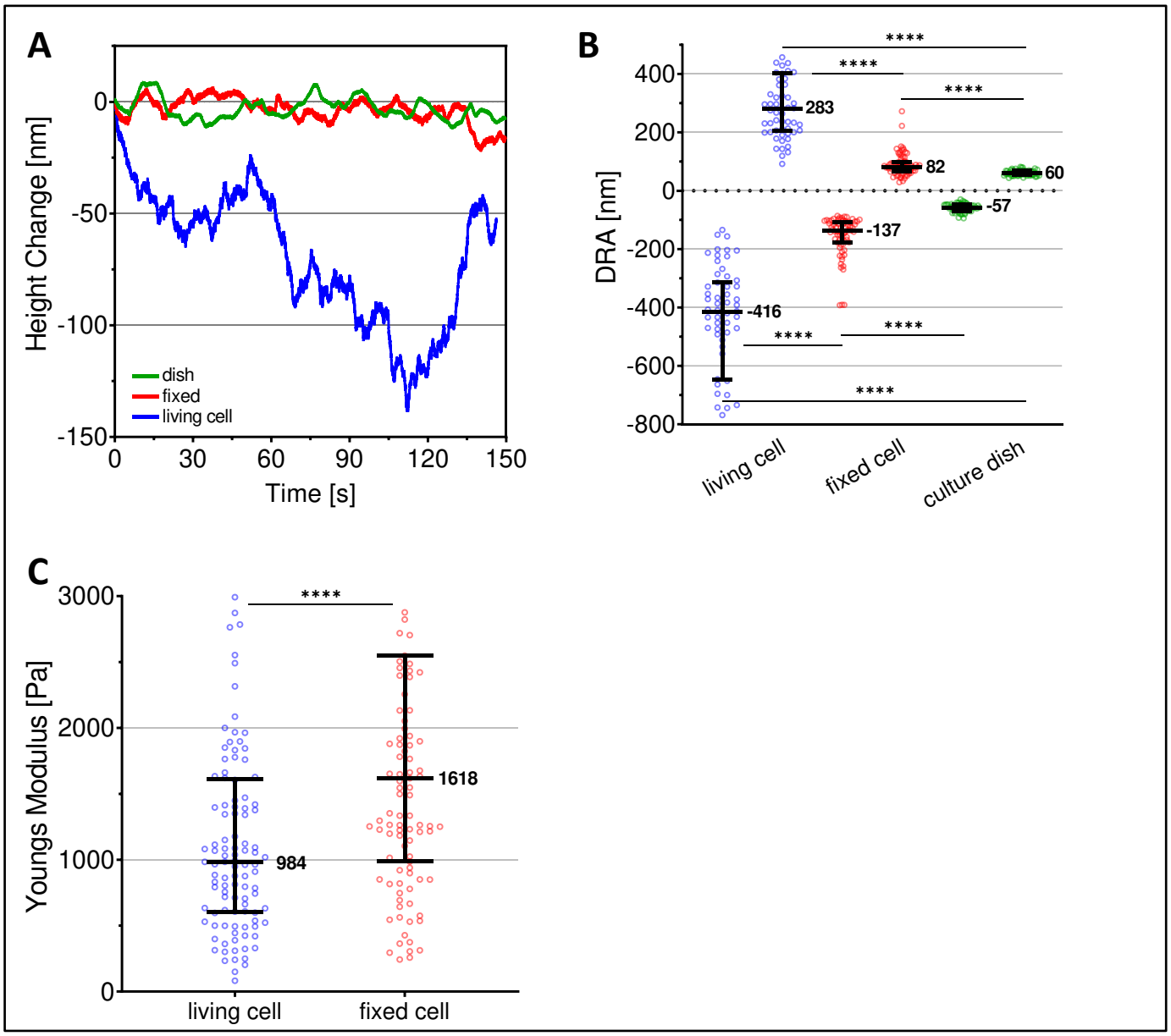

Figure 1. TiMeR detects greater mechanical dynamics in living cells than conventional nanoindentation. a, Representative TiMeR height traces recorded for 150 s under constant load on a living HMEC-1 cell, a PFA-fixed HMEC-1 cell and a cell-free culture dish. Living cells showed larger height excursions than fixed cells or dish-only controls. b, Cumulative positive and negative height changes over 150 s, termed dynamic response amplitude (DRA). Each trace contributed one positive and one negative DRA value corresponding to the summed upward and downward height changes during the recording period. Median DRA values were −416 nm and +283 nm for living cells, −137 nm and +82 nm for fixed cells, and −57 nm and +60 nm for dish controls. c, Young's modulus determined by conventional AFM nanoindentation for living and PFA-fixed cells. The median value increased from 984 Pa for living cells to 1618 Pa for fixed cells, approximately 65% higher. The modulus of the bare culture dish was not measurable within the cellular range and is not shown. n = 58 living cells, n = 73 fixed cells and n = 60 dish controls from independent TiMeR recordings; n = 109 living cells and n = 107 fixed cells from independent nanoindentation measurements. ****p < 0.0001, Mann-Whitney U test.

Figure 2

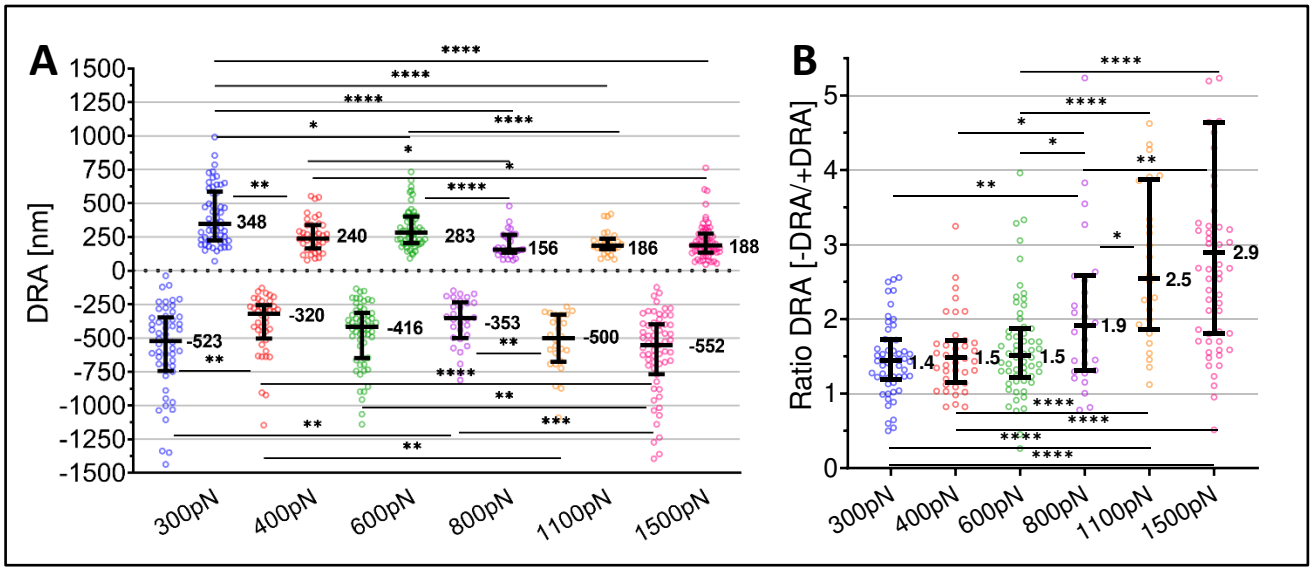

Figure 2. Cells maintain a mechanodynamic balance at intermediate loads. a, Dynamic response amplitudes measured in HMEC-1 cells over 150 s under constant loads ranging from 300 to 1500 pN. Median −DRA/+DRA values were −523/+348 nm at 300 pN, −320/+240 nm at 400 pN, −416/+283 nm at 600 pN, −353/+156 nm at 800 pN, −500/+186 nm at 1100 pN and −552/+188 nm at 1500 pN. Positive DRAs showed a significant inverse correlation with applied force (Spearman's ρ = −0.37, p < 0.0001). b, Ratio of −DRA to +DRA across the applied load range. The median ratio remained 1.4–1.5 between 300 and 600 pN and increased progressively at higher loads, reaching 2.9 at 1500 pN, consistent with a shift toward relaxation-dominated dynamics. n = 54, 40, 58, 30, 26 and 63 independent TiMeR recordings at 300, 400, 600, 800, 1100 and 1500 pN, respectively. *p < 0.05; **p < 0.01; ***p < 0.001; ****p < 0.0001, Mann-Whitney U test.

Figure 3

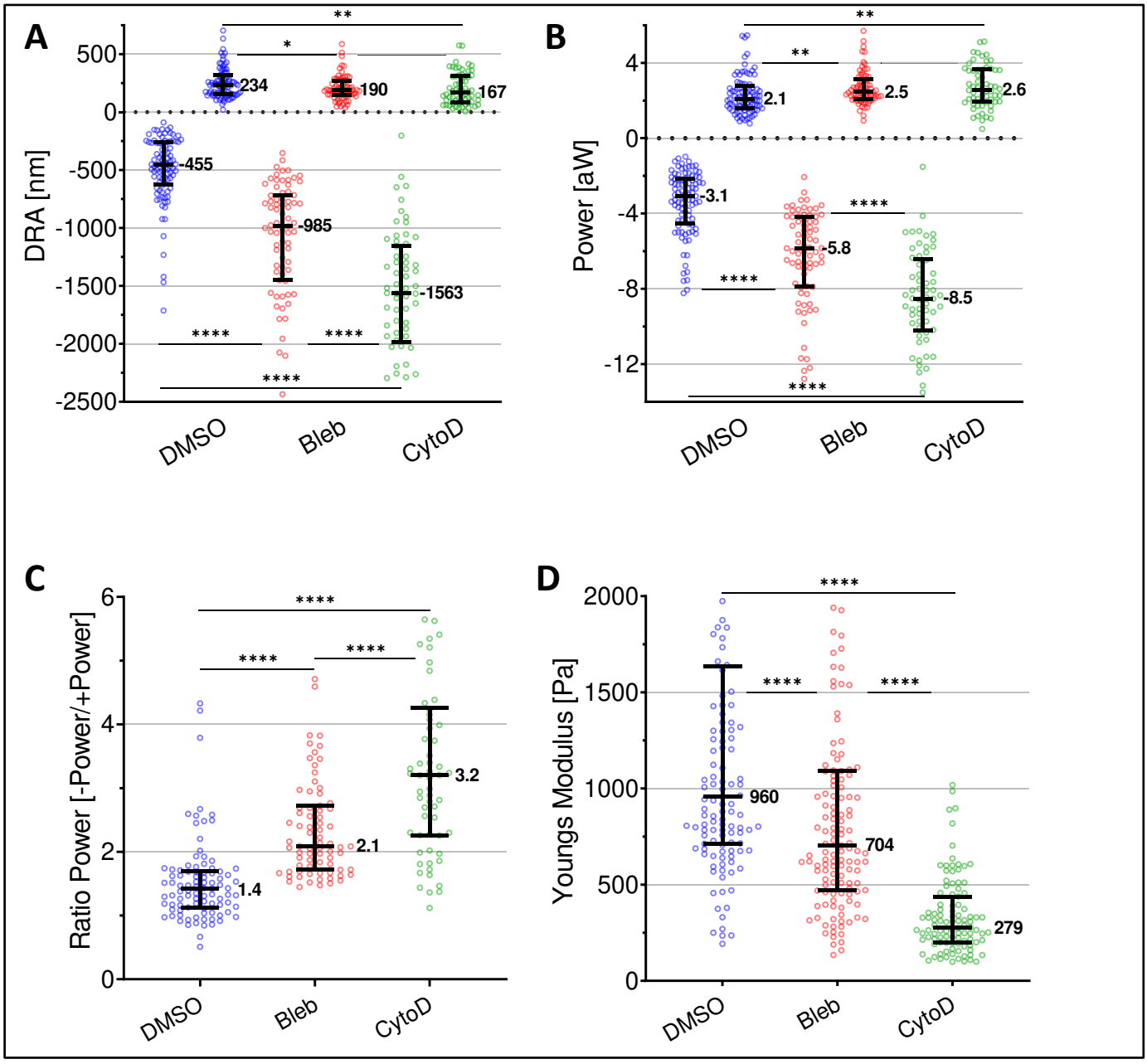

Figure 3. Perturbation of the actomyosin network shifts cellular mechanodynamics toward relaxation and reduces elasticity. a, Dynamic response amplitudes measured in HMEC-1 cells treated with vehicle control (DMSO), blebbistatin or cytochalasin D. Median −DRA/+DRA values were −455/+234 nm for control cells, −985/+190 nm after blebbistatin treatment and −1563/+167 nm after cytochalasin D treatment. b, Power associated with negative and positive height changes under the same conditions. Median negative/positive power values were −3.1/+2.1 aW for control cells, −5.8/+2.5 aW after blebbistatin treatment and −8.5/+2.6 aW after cytochalasin D treatment. c, Ratio of negative to positive power for individual cells. Median ratios increased from 1.4 in control cells to 2.1 after blebbistatin treatment and 3.2 after cytochalasin D treatment. d, Young's modulus determined by conventional AFM nanoindentation. Median values were 960 Pa for control cells, 704 Pa after blebbistatin treatment and 279 Pa after cytochalasin D treatment. For TiMeR measurements, n = 93, 75 and 62 independent recordings; for nanoindentation, n = 124, 131 and 103 independent measurements for control, blebbistatin- and cytochalasin D-treated cells, respectively. *p < 0.05; **p < 0.01; ***p < 0.001; ****p < 0.0001, Mann-Whitney U test.

Figure 4

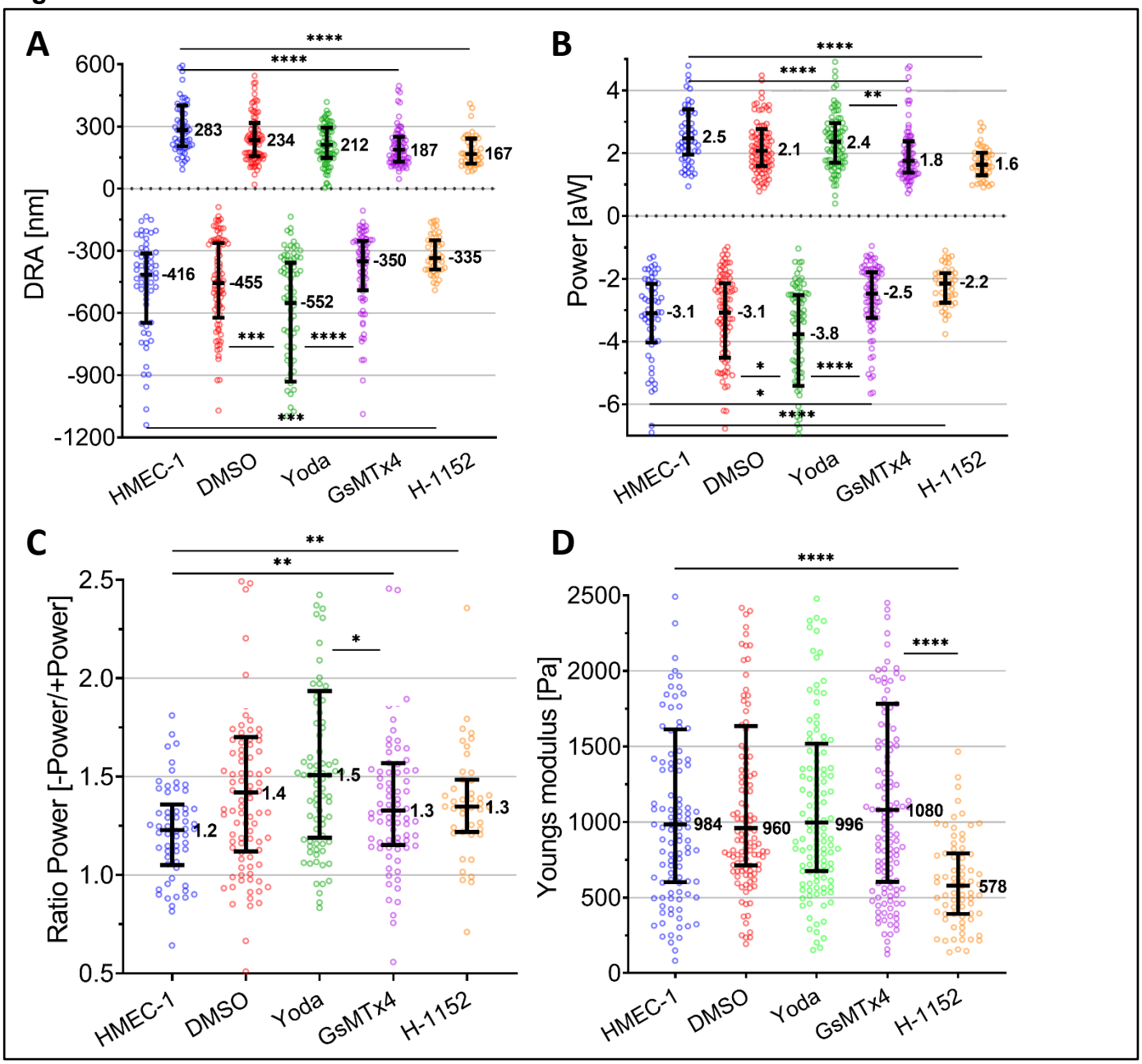

Figure 4. Mechanosensitive signaling and ROCK regulate cellular mechanodynamics. a, Dynamic response amplitudes measured in HMEC-1 cells after treatment with Yoda1, GsMTx4 or H-1152. Median −DRA/+DRA values were −416/+283 nm for HMEC-1 cells, −455/+234 nm for HMEC-1 with vehicle control (DMSO), −552/+212 nm for Yoda1, −350/+187 nm for GsMTx4 and −335/+167 nm for H-1152. b, Power associated with negative and positive height changes under the same conditions. Median negative/positive power values were −3.1/+2.5 aW for HMEC-1, −3.1/+2.1 aW for DMSO, −3.8/+2.4 aW for Yoda1, −2.5/+1.8 aW for GsMTx4 and −2.2/+1.6 aW for H-1152. c, Ratio of negative to positive power for individual cells. Median ratios were 1.2 for HMEC-1, 1.4 for DMSO, 1.5 for Yoda1, 1.3 for GsMTx4 and 1.3 for H-1152. d, Young's modulus determined by conventional AFM nanoindentation. Median values were 984 Pa for HMEC-1, 960 Pa for DMSO, 996 Pa for Yoda1, 1080 Pa for GsMTx4 and 578 Pa for H-1152. For TiMeR measurements, n = 58, 93, 85, 80 and 43 independent recordings for HMEC-1, DMSO, Yoda1, GsMTx4 and H-1152, respectively; for nanoindentation, n = 109, 124, 126, 135 and 71 independent measurements for the same conditions. *p < 0.05; **p < 0.01; ***p < 0.001; ****p < 0.0001, Mann-Whitney U test.

Figure 5

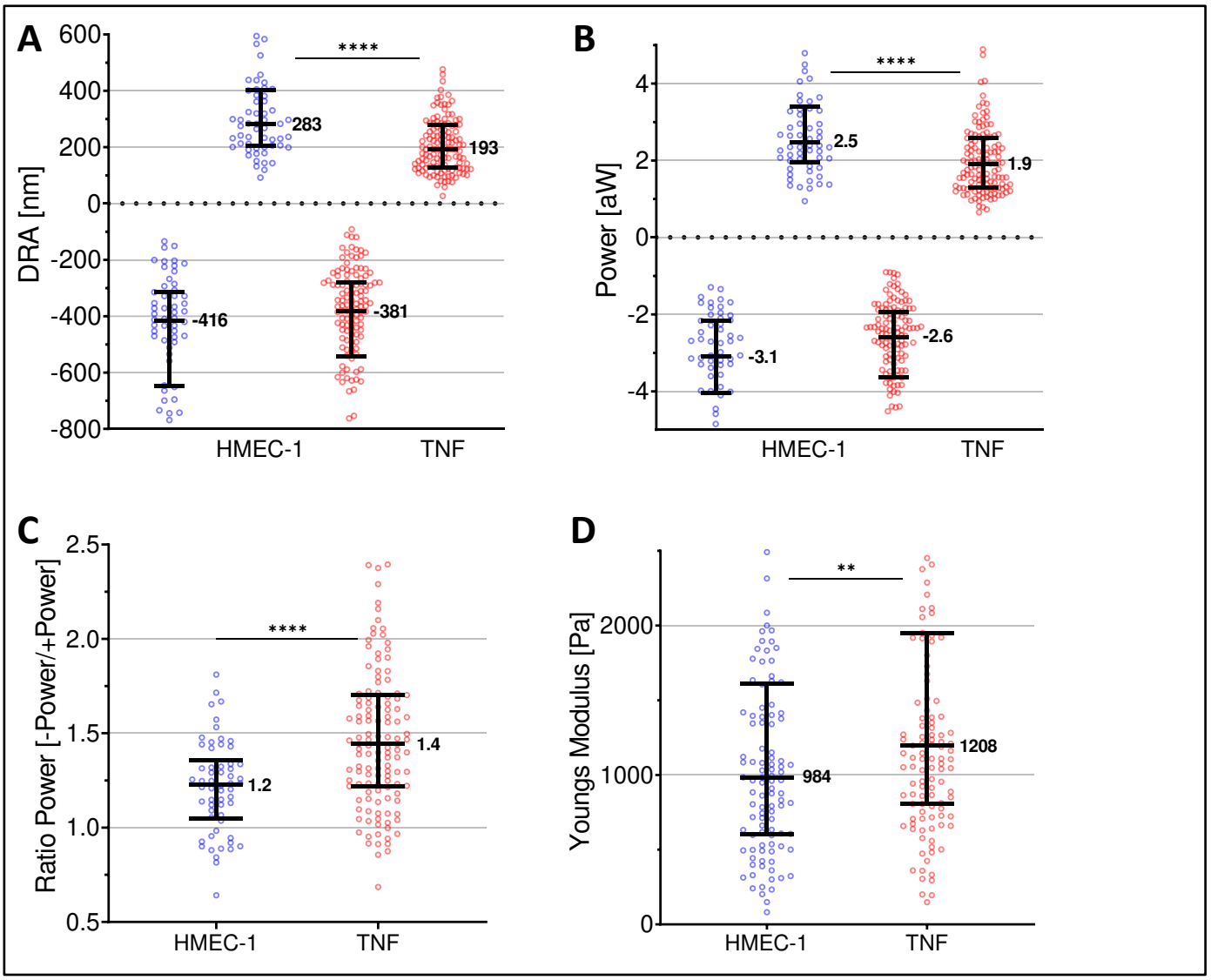

Figure 5. TNF-α shifts endothelial mechanodynamics toward relaxation. a, Dynamic response amplitudes measured in HMEC-1 cells after TNF-α treatment or in untreated control cells. Median −DRA/+DRA values were −416/+283 nm for control cells and −381/+193 nm after TNF-α treatment, corresponding to a 32% reduction in push-associated DRA. b, Power associated with negative and positive height changes under the same conditions. Median negative/positive power values were −3.1/+2.5 aW for control cells and −2.6/+1.9 aW after TNF-α treatment, corresponding to a 25% reduction in push-associated power. c, Ratio of negative to positive power for individual cells. Median ratios were 1.2 for control cells and 1.4 after TNF-α treatment. d, Young's modulus determined by conventional AFM nanoindentation. Median values were 984 Pa for control cells and 1208 Pa after TNF-α treatment. For TiMeR measurements, n = 58 and 130 independent recordings for control and TNF-α-treated cells, respectively; for nanoindentation, n = 109 and 123 independent measurements for the same conditions. *p < 0.05; **p < 0.01; ***p < 0.001; ****p < 0.0001, Mann-Whitney U test.

Figure 6

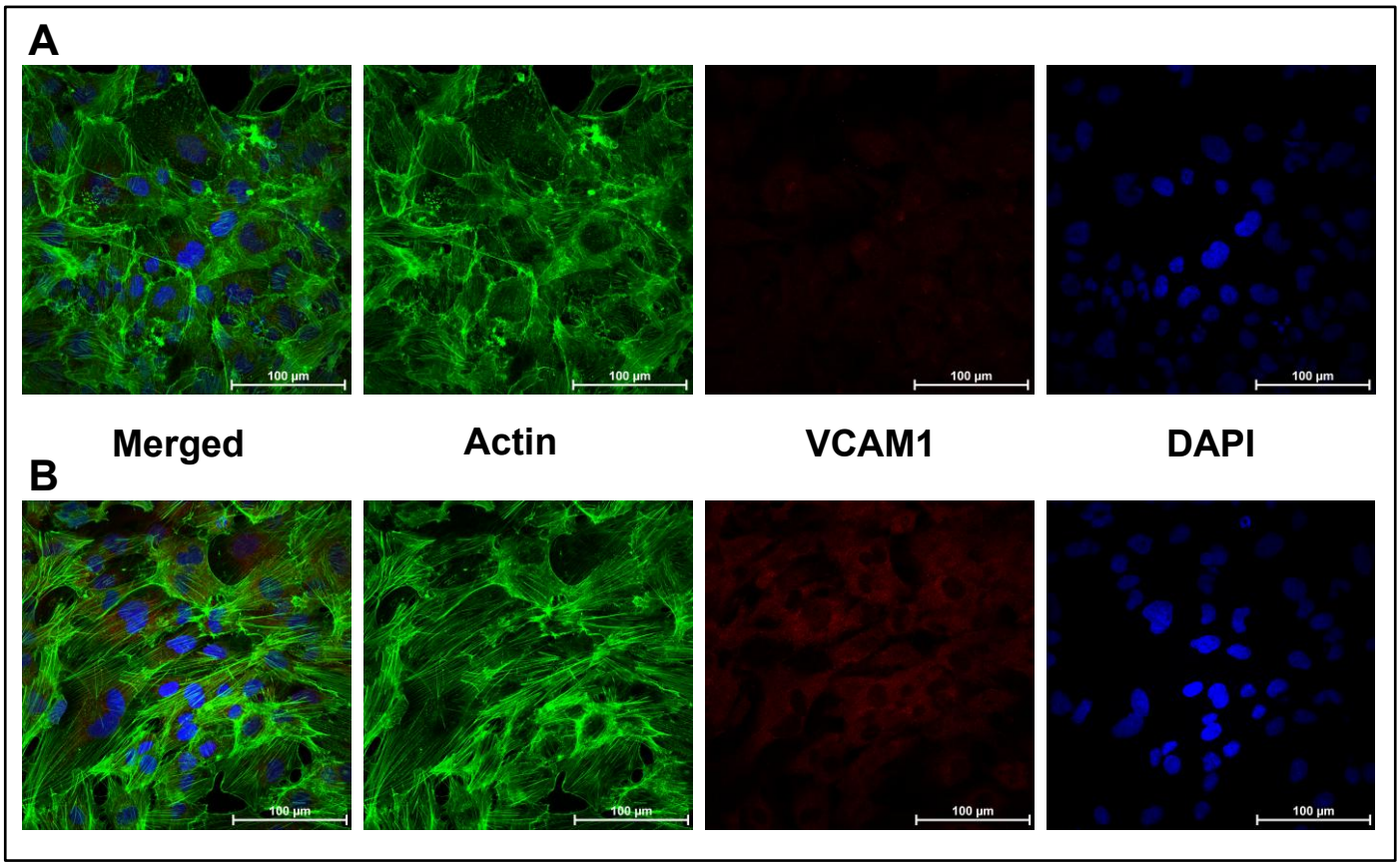

Figure 6. Changes in the actin network and VCAM1 immunofluorescence signal of TNF-α–treated HMEC-1 cells compared with untreated cells. Each row shows, from left to right: merged channels, filamentous actin (Phalloidin, green), VCAM1 immunofluorescence signal (red) and nuclear counterstain (DAPI, blue). Top row: untreated control cells show sporadic actin stress fibers and low VCAM1 immunofluorescence signal. Bottom row: TNF-α–treated cells (10 ng ml^{-1}; 24 h) show substantially higher VCAM1 immunofluorescence signal and pronounced actin stress fiber formation compared with control cells. Scale bar: 100 µm.

Figure 7

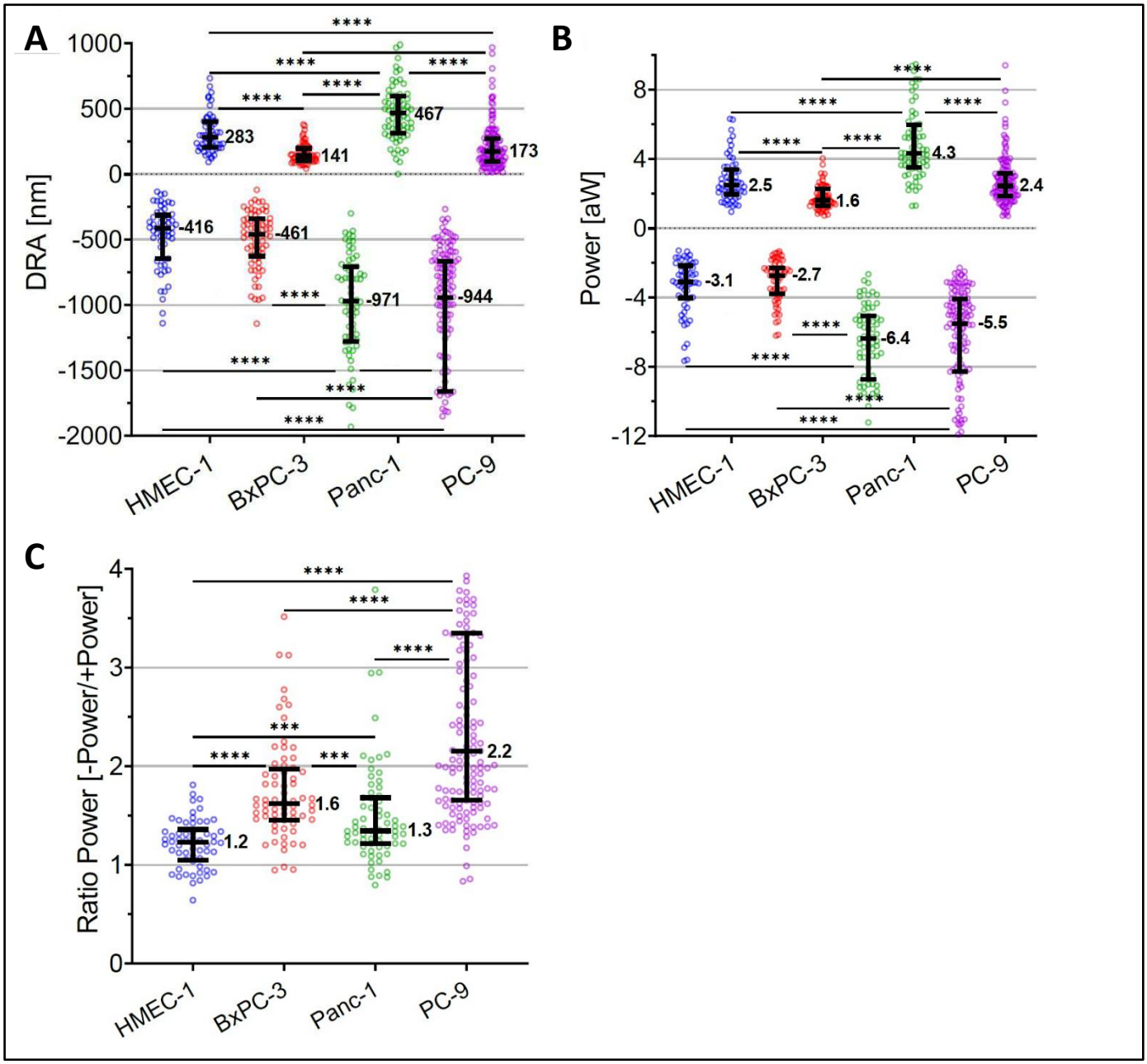

Figure 7. TiMeR resolves distinct mechanodynamic profiles across different cell lines. a, Dynamic response amplitudes measured in untreated HMEC-1, BxPC-3, Panc-1 and PC-9 cells under the same conditions. Median −DRA/+DRA values were −416/+283 nm for HMEC-1 cells, −461/+141 nm for BxPC-3 cells, -971/+467 nm for Panc-1 cells and -944/+173 nm for PC-9 cells. b, Power associated with negative and positive height changes under the same conditions. Median negative/positive power values were −3.1/+2.5 aW for HMEC-1 cells, −2.7/+1.6 aW for BxPC-3 cells, −6.4/+4.3 aW for Panc-1 cells and -5.5/+2.4 aW for PC-9 cells. c, Ratio of negative to positive power for individual cells. Median ratios were 1.2 for HMEC-1 cells, 1.6 for BxPC-3 cells, 1.3 for Panc-1 cells and 2.2 for PC-9 cells. For TiMeR measurements, n = 58, 68, 67 and 144 independent recordings were obtained for HMEC-1, BxPC-3, Panc-1 and PC-9 cells, respectively. *p < 0.05; **p < 0.01; ***p < 0.001; ****p < 0.0001, Mann-Whitney U test.